JGR Planets

RESEARCH ARTICLE
10.1029/2021JE007159

Stability of the Jupiter Southern Polar Vortices Inspected Through Vorticity Using Juno/JIRAM Data

P. Scarica[1], D. Grassi[1], A. Mura[1], A. Adriani[1], A. Ingersoll[2], C. Li[3], G. Piccioni[1], G. Sindoni[4], M. L. Moriconi[5], C. Plainaki[4], F. Altieri[1], A. Cicchetti[1], B. M. Dinelli[6], G. Filacchione[1], A. Migliorini[1], R. Noschese[1], R. Sordini[1], S. Stefani[1], F. Tosi[1], and D. Turrini[1]

[1]Istituto di Astrofisica e Planetologia Spaziali-Istituto Nazionale di Astrofisica, Rome, Italy, [2]Division of Geological and Planetary Sciences, California Institute of Technology, Pasadena, CA, USA, [3]Department of Climate and Space Sciences and Engineering, University of Michigan, Ann Arbor, MI, USA, [4]Agenzia Spaziale Italiana, Sede di Roma, Rome, Italy, [5]Istituto di Scienze Atmosferiche e del Clima, Consiglio Nazionale delle Ricerche, Sede di Roma, Rome, Italy, [6]Istituto di Scienze Atmosferiche e del Clima, Consiglio Nazionale delle Ricerche, Sede di Bologna, Bologna, Italy

Key Points:

- The vorticity field of Jupiter's southern polar cyclones is evaluated for different orbits
- The temporal variability of the vorticity field of the central polar cyclone is analyzed
- We found extremely long stability of the morphology of circumpolar cyclones both in terms of clouds and winds

Correspondence to:
P. Scarica,
pietro.scarica@inaf.it

Citation:
Scarica, P., Grassi, D., Mura, A., Adriani, A., Ingersoll, A., Li, C., et al. (2022). Stability of the Jupiter southern polar vortices inspected through vorticity using Juno/JIRAM data. *Journal of Geophysical Research: Planets*, *127*, e2021JE007159. https://doi.org/10.1029/2021JE007159

Received 16 DEC 2021
Accepted 30 JUN 2022

Abstract The Jovian InfraRed Auroral Mapper (JIRAM) onboard the NASA Juno mission monitored the evolution of Jupiter's polar cyclones since their first observation ever in February 2017. Data acquired by JIRAM have revealed cloudy cyclones organized in a complex, yet stable geometrical pattern at both poles. Several studies have investigated the dynamics and the structure of these cyclones, to understand the physical mechanisms behind their formation and evolution. In this work, we present vorticity maps deduced from the wind fields for the region poleward of ∼−80°, which has been extensively covered over the last four years of observations. The cyclonic features related to the stable polar cyclones are embedded in a slightly, but diffused anticyclonic circulation, in which short-living anticyclones emerge with respect to the surroundings. Although the general stability of both the cyclones and the whole system is strongly confirmed by this work, variations in the shape of the vortices, as well as changes in the local structures, have been observed.

Plain Language Summary The Jovian InfraRed Auroral Mapper is the instrument onboard the NASA Juno spacecraft that has provided observations of Jupiter's poles since February 2017. These data have shown cyclones organized in snowflake-like structures. The Jupiter's polar cyclones are long-lasting features, which did not disappear or merge during 4 years of observations. In general, the analysis of the winds is important in the study of the cyclones. In this work, we focus on the vorticity, a quantity derived by the winds, that gives information on the magnitude and direction of the rotation of the cyclones. We focused on the southern polar region, which has a better coverage in time, with respect to the northern counterpart. The general pattern of the southern polar cyclones is preserved along the observations.

1. Introduction

Jupiter's poles host systems of stable vortices clustered in a limited region poleward of ±80°, which do not merge (Adriani et al., 2018). These systems of vortices have been detected for the first time thanks to the NASA Juno mission (Bolton et al., 2017); the unfavorable viewing angles of ground-based observations (Hueso et al., 2017), and past space missions' trajectories at Jupiter, for example, Galileo (Carlson et al., 1992), Cassini (Coradini et al., 2004) and NewHorizons (Baines et al., 2007; Reuter et al., 2007) prevented previous detections. First polar cyclones full-view observations were returned from JIRAM (the Jovian InfraRed Auroral Mapper onboard Juno; Adriani et al., 2017), which is an IR spectral-imaging instrument. The observed vortices display geometrical symmetries around both poles: circumpolar cyclones (CPCs), organized in a regular pattern, surround a central one. At the north pole, eight circumpolar vortices form an octagonal structure, while at the south pole, five circumpolar vortices are arranged in a pentagonal pattern; both central polar vortices show some degree of displacements to the geometrical pole, about 0.5° for the Northern Polar Cyclone (NPC) and 1°–2° for the SPC.

Although some perturbations and changes in the geometrical pattern have been reported (Adriani et al., 2020; Mura et al., 2021), the general stability of these close-clustering cyclones is inferred thanks to data acquired along the lifespan of the Juno mission. Since PeriJove 4 (PJ 4, which is the fourth orbit of Juno around Jupiter), the SPC and its five CPCs show radii spanning from 2,800 to 3,500 km, with a certain degree of variability in the morphology of each cyclone. Meanwhile, short-living and relatively small anticyclones emerge and disappear

within a single PeriJove passage (53 days), developing among the cyclones or just equatorward of the −80° parallel. At the same time, the NPC and its eight CPCs show radii spanning from 2,000 to 2,300 km, with different morphologies and cloudiness of the cyclones; however, due to the JIRAM coverage of the North pole, the evolution of this polar region could not be monitored as extensively as its southern counterpart.

The physics behind the formation of cyclones and anticyclones, as well as their drifting patterns in a planetary atmosphere, has long been investigated. In the hypothesis of geostrophic turbulence, large-scale structures like vortices originate from small-scale turbulences through an inverse-cascade process (Vallis, 2017). Therefore cyclones, rotating clockwise in the southern hemisphere of a planet and anticlockwise in the northern hemisphere, cluster at high latitudes thanks to the β-effect associated with a revolving sphere (Schecter & Dubin, 1999); conversely, anticyclones, rotating anticlockwise in the southern hemisphere of a planet and clockwise in the northern hemisphere, tend to accumulate around the equator for the same β-effect. Indeed, due to this non-linear phenomenon, vortices interact with the surrounding vorticity, with a strength proportional to β, the meridional gradient of the Coriolis parameter, leading to westward-poleward driven cyclones and westward-equatorward driven anticyclones. CPCs are denied moving further toward the poles, due to the antivorticity field surrounding the central polar cyclones (Li et al., 2020). Assuming an alternative formalism based on the barotropic approximation, CPCs stabilize in an equilibrium state centered at a given parallel, as an effect of the vorticity gradient of the central polar cyclones (Gavriel & Kaspi, 2021).

The complexity of the systems of cyclones appearing at both poles of Jupiter becomes even more puzzling in comparison with Saturn, the other gas giant planet of the Solar System, which displays just one big cyclone over each pole (Baines et al., 2009): this difference underlines a diverse physical mechanism working on the two planets or profound differences in the fluid dynamics parameters.

In this scenario, several modeling attempts have been made to reproduce the observed features, both through "shallow" and "deep" approaches.

The model presented in O'Neill et al. (2015) reproduced vortices near the pole of Jupiter in a shallow-water approximation and showed the different evolution paths followed by cyclones and anticyclones, which drift toward the poles and the equator, respectively; it also demonstrated the dependence between the number of polar-circumpolar vortices and the Burger number (defined as the square of the Rossby deformation radius divided by the planetary radius). The numerical simulation published in Brueshaber et al. (2019) confirmed the correlation of the number of polar-circumpolar vortices and the Burger number, with high Burger numbers ($>10^{-3}$) corresponding to a strong pole-centered cyclone; morphologies like the one observed on Saturn have been also reproduced, as well as the Jupiter polar-circumpolar structure. Li et al. (2020) modeled the drift of cyclones toward the pole and their tendency to group into regular polygonal patterns, whose stability is maintained by an anticyclonic ring of vorticity surrounding cyclones.

Considering a deep rotating convection zone, several models were able to generate long-living vortices (Guervilly & Hughes, 2017; Yadav et al., 2020). In particular, Garcia et al. (2020) explained the presence of a single strong polar vortex on Saturn and multiple cyclones on Jupiter as a function of the Rayleigh number. Invoking the inertial stability criterion (Yanai, 1964), Cai et al. (2021) were able to pack cyclones that do not merge, under the hypothesis of a high Coriolis parameter; they also confirmed the role of the Rossby number and the role of the lateral-to-height aspect ratio in the general structure of polar cyclones. Rubio et al. (2014) studied the formation—in a geostrophic turbulence scenario—of large-scale coherent structures surrounding the rotation axis, where the energy source for these large-scale barotropic components is provided by small scale convective eddies.

Although these numerical simulations brought fundamental advancements in the understanding of the mechanisms behind the observed vortices structure, there are still aspects to be clarified. Some of these controversial aspects, like the long-time stability of the polar vortices structure, as well as the lack of accumulation or merging of these vortices, are starting to be reproduced by models. However, to validate such models, comparisons with data are fundamental.

Based on the tracking of atmospheric features (cloud tracking), Grassi et al. (2018) retrieved wind speeds at ∼1 bar level using the infrared images acquired by JIRAM at 4.54–5.03 μm, during PJ 4, for both northern and southern polar regions. The peak speeds for each cyclone were roughly located at 1,000 km from the centers. This study highlighted speeds exceeding 80 m/s within several cyclones, with peaks over 100 m/s, while anticyclonic

features were identified across both polar regions. The sampling steps between the pair of images adopted in the analysis allowed a minimum detectable speed of 12 m/s at the north pole and 9.6 m/s at the south pole.

Siegelman et al. (2021) focused on the northern polar region observed by JIRAM during PJ 4 and detected wind speeds peaking at about 100 m/s within circumpolar vortices. Wind measurements highlighted a turbulent regime, which involved two classes of vortices: small-scale dynamics are driven by vertical motions, while large-scale dynamics associated with vortices are driven by horizontal motions.

Ingersoll et al. (2021) presented a different retrieval of the vorticity field for the northern polar region during PJ 4, as observed by JIRAM, from which small-scale structures emerge in the vorticity maps. The analysis remarks the importance of convection, inferred as the primary source of energy in Jupiter's atmosphere dynamics.

The work that we present here evolves from Grassi et al. (2018) and it has been conducted thanks to JIRAM data acquired during several Juno orbits, from PJ 4 (February 2017) to PJ 33 (April 2021). Through this study, we present an extensive analysis of the southern polar region of Jupiter: in particular, vorticity maps are deduced from the wind fields. Thanks to the JIRAM data set spanning 4 years, the time variability of these vorticity maps highlights both the general stability of the southern polar cyclonic region and the local changes in the dynamics of cyclones.

In the following section (Section 2), we introduce the JIRAM instrument and its data set, with a focus on the data used in this analysis. In Section 3, we present the method adopted to estimate the winds. In Section 4, vorticity maps for the southern hemisphere are discussed, with a particular focus on the stability of the polar cyclonic region displayed along different PJ passages and the local changes observed across these maps, in both the cyclonic and anticyclonic features.

2. Data

The JIRAM instrument onboard Juno is devoted to the study of the Jovian atmosphere and aurorae. It includes a spectrometer and an IR imager. The spectrometer operates in the 2.0–5.0 μm interval. The IR imager is divided into two spectral channels: the L-band, centered at 3.45 μm, is characterized by a bandwidth of 0.29 μm, while the M-band, centered at 4.78 μm, is characterized by a bandwidth of 0.48 μm. Images are acquired simultaneously by the IR imager and are stored into matrixes of 432 × 128 pixels (Adriani et al., 2017). The individual field of view of each pixel is 240 μrad and the FOV of the images is 1.75° × 5.94°. Each image is acquired every 30 s, for example, at a different rotation of the Juno spacecraft; a set of consecutive images, collected along the same PJ passage, is called "a sequence." Sequences of images are planned to compose a mosaic of a given region. Due to the polar orbit of the Juno spacecraft, polar regions are visible, although the level of detail (the pixel spatial resolution) and the spatial coverage depend on the distance between the spacecraft and the planet. In general, the southern polar region offers better spatial coverage than its northern counterpart.

In this work, we focus on M-band data that are acquired by integrating the incoming radiance over the 4.54–5.03 μm range (roughly corresponding to 1–2 bar pressure), and in particular on the sequences of images acquired at high latitudes (roughly poleward of −80°) in the southern hemisphere.

3. Methods

The work that we present here follows Grassi et al. (2018), from which it derives the adopted algorithm, although having its major focus on the vorticity maps rather than wind speeds maps. Hereafter, we present the general idea behind the retrieval method, along with the changes in the algorithm with respect to Grassi et al. (2018). For further details regarding the retrieval method, we refer to Grassi et al. (2018), in which a more extended characterization of the algorithm is given.

The process of wind speeds retrieval that we use, based on cloud tracking principles, compares JIRAM M-band images belonging to different image sequences. Thus, pairs of images are formed (one from the first sequence, one from the second sequence). These images, acquired at different times, are interpolated over a grid of 11.6 km sampling step (0.01° of latitude). Only overlapping images are selected, while those pairs that do not cover the same geographical region of Jupiter, are discarded.

Table 1
List of the Selected Jovian InfraRed Auroral Mapper M-Band Image Sequences Presented in This Work

PJ passages	First sequence	Second sequence	Time separation (s)	Pixel resolution (km)
PJ 4	170202_140125	170202_142113	1,188	21.6–33.2
PJ 28	200725_074625	200725_075426	481	31.1–35.3
PJ 28	200725_075025	200725_075826	481	32.7–36.9
PJ 28	200725_075426	200725_080227	481	34.3–38.4
PJ 28	200725_075826	200725_080657	511	35.9–40.3
PJ 28	200725_080227	200725_081058	511	37.5–41.7
PJ 28	200725_080657	200725_081458	481	39.2–43.2
PJ 28	200725_081058	200725_081859	481	40.8–44.8
PJ 28	200725_081458	200725_082259	481	42.3–46.3
PJ 30	201108_034202	201108_034703	301	39.5–42.4
PJ 30	201108_034703	201108_035504	481	41.4–45.4
PJ 30	201108_035504	201108_040305	481	44.4–48.4
PJ 33	210416_005425	210416_010326	511	27.4–31.9
PJ 33	210416_005925	210416_010757	511	29.2–33.7
PJ 33	210416_010326	210416_011157	511	30.8–35.2
PJ 33	210416_010757	210416_011558	481	32.7–36.6

Note. The first column identifies the Juno orbit (the PJ passage). "First sequence" and "Second sequence" columns report the file name of the sequences: each of the rows is related to one of the pairs processed by the retrieval algorithm. The time separation indicates the time gap between the sequences of that pair. The last column indicates the range of the pixel resolution.

Atmospheric features—clouds—are identified in terms of their radiance. The motions of the clouds are tracked over the two images: the algorithm, based on the Mean Absolute Distortion (MAD), as defined in Gonzalez and Woods (2008), finds the best matching bidimensional displacement vector between the first and the second image. This vector is searched in a squared neighborhood centered over each pixel. Knowing the best-matching vector and considering the time gap between images, the local wind speed is retrieved for each of the pixels. The borders of the images are excluded to prevent the algorithm from searching outside the images. After evaluating all the pixels, the procedure allows to compute the wind field for the entire image; by stacking sequences of images belonging to the same PJ passage data set, a wind field mosaic is obtained. In this study, phenomena such as sublimation or condensation are not considered, as well as small-scale rotations and changes of the cloud features due to wave activity.

Being the nominal pointing uncertainty of JIRAM images about one pixel, the minimum pointing uncertainty in this study is roughly 11.6 km. In Grassi et al. (2018), the bidimensional displacement vector was defined in terms of integer numbers of sampling steps along both axes. Thus, the optimal displacement deduced by the algorithm was a multiple of the sampling step. In the present work, after deducing the best matching bidimensional displacement vector between images, a bidimensional gaussian fit is produced over a region of 5×5 pixels, and the position of the estimated peak derived by the MAD function is not linked to the grid sampling steps. Thanks to this change in the algorithm, we can calculate the vorticity field, defined as the curl of the velocity field:

$$\vec{\omega} = \overrightarrow{\nabla} \; x \; \vec{v} \tag{1}$$

Thus, once we derived the wind speeds, we calculated the vorticity field and we produced maps of the vorticity for each of the PJ passages.

Among all JIRAM observations from PJ 4 until PJ 33, we selected a data set consisting of 123 sequences and a total of 1,216 images, which cover the south polar region of Jupiter. However, a preliminary analysis highlighted the need for a more severe selection. Indeed, images separated by a small-time gap, as well as images characterized by a worse spatial resolution, produced poor vorticity maps, because of the larger relative error due to the pointing uncertainty of JIRAM. On the other hand, images separated by a larger time gap, as well as those characterized by a better spatial resolution, produced well-contrasted and coherent vorticity maps. For such a reason, we selected only pairs of images separated by at least 8 min (apart from a sequence of images acquired during PJ 30). It has to be noted that longer time intervals worsen the JIRAM spatial coverage of the south polar region. Indeed, although JIRAM M-band data provided, in general, a good coverage of the south polar region along several PJ passages (polar and CPCs are often observed at least by one JIRAM sequence of images for each PJ passage), our choice to impose a minimum time gap between the sequences of images that we utilized, limits the data set useful to perform the wind retrieval. Moreover, effects due to small-scale rotations and wave activity, that are not considered in this algorithm, may not be negligible for longer time intervals.

In this work we only present vorticity maps related to those PJ passages that display a satisfying spatial coverage after the imposed selection. All the sequences of images utilized in this work are reported in Table 1. Following the idea behind our algorithm, each pair of sequences that have been used is reported on a separate row. From the point of view of the random error, due to the size of the sampling step (11.6 km) and the time gap between images (typically acquired at 8 min apart), the retrieved winds are typically characterized by a minimum detectable speed of roughly 24 m/s, which becomes 48 m/s in the worst-case scenario, corresponding to images acquired at 4 min apart and about 9.6 m/s in the case of PJ 4, whose sequences are separated by roughly 20 min.

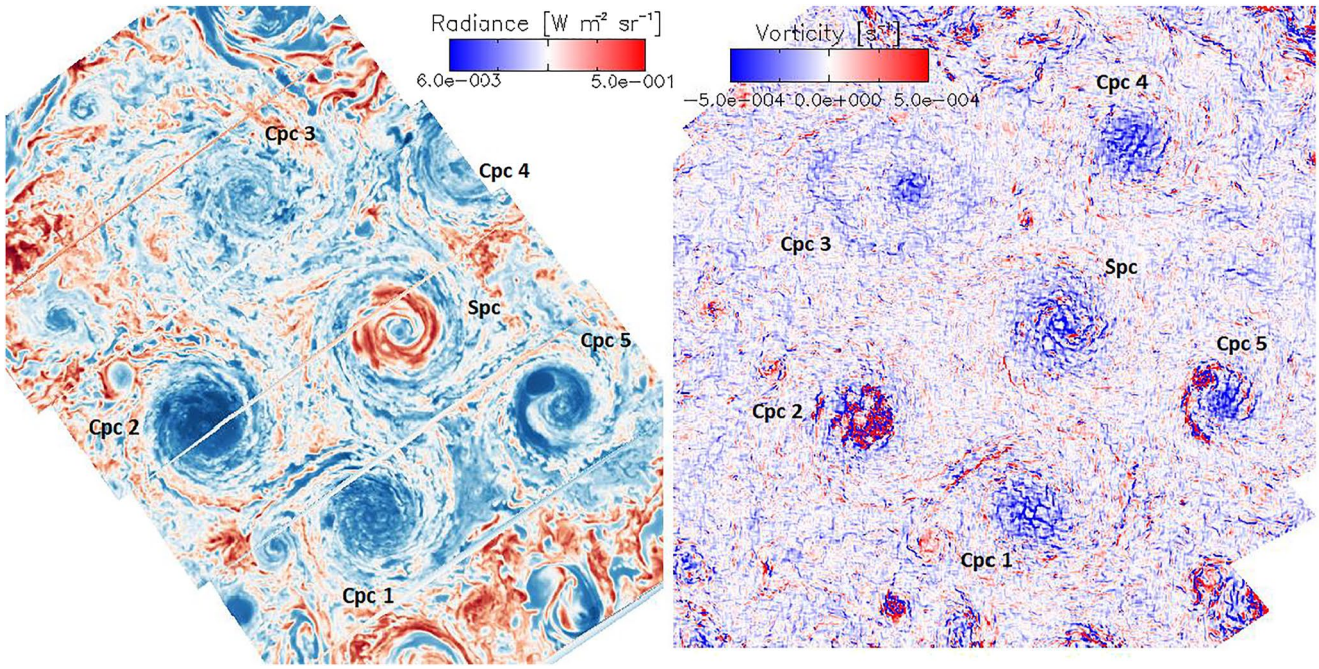

Figure 1. (Left panel) A mosaic of Jovian InfraRed Auroral Mapper images belonging to the "200725_080657" sequence (PeriJove [PJ] 28). The measured radiance spans from 0.006 to 0.5 W m^{-2} sr^{-1}. The logarithmic radiance scale goes from blue to red, where blue corresponds to regions that are colder and darker in the IR, and red corresponds to regions that are warmer and brighter in the IR. The Southern Polar Cyclone can be recognized as a bright vortex in the middle of the image; circumpolar vortices appear as darker, more cloudy cyclones. (Right panel) Vorticity map obtained as a mosaic of the PJ 28 images sequences adopted in this work; positive values of vorticity correspond to antivorticity in the adopted notation. Vorticity in regions covered by multiple, overlapping pairs of sequences, is obtained as an average of the estimated vorticities. A 5 × 5 smoothing has been imposed. CPC means circumpolar cyclone; circumpolar cyclones are clockwise numbered. SPC means Southern Polar Cyclone.

In Grassi et al. (2018), a search area (the neighborhood over which the best matching displacement vector is searched) of 21 × 21 pixels was used. A larger search area requires a longer computational time; however, it also allows a deeper search of the best matching vector in those regions where the algorithm cannot detect a proper matching vector within a smaller search area. For this reason, we only utilized the 21 × 21 pixels search area for the preliminary analysis and then we changed the size of this area to 41 × 41 pixels (the computational time increased by roughly four times). Thus, all the vorticity maps shown hereafter, have been produced with a 41 × 41 pixels search area.

4. Results

The presence of cyclones at both poles of Jupiter, organized in crystal-like structures, finds its physical explanation in the interaction between the vorticity related to vortices and the background vorticity, which increases monotonically toward the poles. Under this scenario, the final position of the vortices fits a physical model (Gavriel & Kaspi, 2021) that depends on the vortices' intensities and sizes with respect to the background vorticity and length scale. Thus, the stability of such a structure is driven by the vorticity between large cyclones and requires cyclonic vortices embedded in an anticyclonic field. The disruption of this pattern would lead to instability and loss of vortices by merging. Moreover, cyclonic motions surrounded by an anticyclonic one are consistent with zero net vorticity.

To assess the vorticity of the Jupiter southern polar structure, in Figure 1 we show a mosaic of PJ 28 vorticity maps (right panel), compared to the radiance measured by JIRAM-M during the 200725_075826 sequence of images (left panel), which belongs to the PJ 28 data set. It must be noted that the vorticity map in Figure 1 is made of several PJ 28 images sequences; thus, it includes regions that are not covered by the 200725_075826 images sequence.

The observed radiance reveals a Southern Polar Cyclone (labeled SPC) characterized by a darker central spot (blue color) and a brighter periphery (red color), which reaches 0.33 W m^{-2} sr^{-1}. The SPC is surrounded by more turbulent CPCs. CPC 1 and CPC 3 are cloudy cyclones, with a lower average radiance than the SPC; CPC 3, in particular, displays a more irregular shape. CPC 4, on the top right of the image, is only partially observed during this sequence, although it has been investigated thanks to other sequences belonging to PJ 28. Both CPC 2 and CPC 4 are even more cloudy than the other southern CPCs and display the lowest values of radiance (0.006 and 0.008 W m^{-2} sr^{-1}, respectively, in their darkest regions). However, they are very different in shape and size: the larger CPC 2 is circular, the smaller CPC 4 resembles a spiral. Turbulent dynamics dominate equatorward of the −80° latitude mark, where radiance is in general higher than within the polar CPCs region.

Vorticity in Figure 1 goes from blue ($-5 * 10^{-4}$ to 0 s^{-1}) to red (0 to $5 * 10^{-4}$ s^{-1}). In this notation, as we are focusing on the southern polar region, negative vorticity corresponds to cyclones, while positive vorticity corresponds to anticyclones. As expected, the main cyclones (both polar and circumpolar) are dominated by cyclonic motions. Instead, the clouds surrounding the cyclones display a dominant, slightly positive vorticity. From a general perspective, the observed stability of the polar structure (at least in the more than 4 years' time scale that we are aware of) is coherent with this vorticity map, with antivorticity acting as a stabilizer for the general structure of the main cyclones and preventing the merging of these cyclones.

The SPC maintains its visual symmetry in the vorticity map: it appears as a cyclonic, coherent vortex, which presents a slightly higher vorticity in the inner region. An anticyclonic ring surrounds it, with small-scale features associated with an anticlockwise motion. Similar behavior is also found in the case of CPC 1 and CPC 4. CPC 3 shows two rings of cyclonic motions, separated by a narrow annulus of lower vorticity (in terms of absolute values); data acquired during other PJ passages allow to deeply test this peculiarity. CPC 5 is smaller than the other main cyclones in this vorticity map; a visual comparison correlates the darker clouds within the spiral arm with the red, anticyclonic motion that we retrieve in its periphery.

CPC 2 shows a very noisy core with respect to its outer rim, which is dominated by a cyclonic motion. Despite this puzzling behavior, also CPC 2 is surrounded by an antivorticity ring, which encircles both the chaotic core and the cyclonic outer-rim; this fact may suggest a peculiar structure of this cyclone, rather than differences in its interaction with the surroundings. However, it must be noted that a visual comparison with JIRAM images (left panel) reveals a darker region within the CPC 2, with radiance values within that region about 10^{-3} W m^{-2} sr^{-1} (the minimum being roughly 0.006 W m^{-2} sr^{-1}). This radiance is orders of magnitude higher than the Noise Equivalent Radiance (NER) of the instrument (Mura et al., 2017), but may be still troublesome for the cloud tracking. Indeed, a visual inspection of the CPC 2 does not show counter-rotating bright structures within the core of this cyclone. Hence, this puzzling feature may be induced by the absence of features rather than an intrinsic peculiarity in the dynamics of the cyclone: this feature raises a flag about the wind retrieval in those regions characterized by an extremely low and homogeneous (poorly characterized in terms of features) radiance, which is indeed quite unavoidable. However, in the future, JIRAM will increase the coverage of the CPC 2 in order to have more data about this puzzling feature. Infact, papers such that those of Garcia et al. (2020), show that a ring of antivorticity surrounded by a cyclonic motion have been already reproduced in their convective deep modeling. So, even if we don't completely rule out the possibility that this can be confirmed in the future, so far it is not possible to draw a final statement.

The presence of an anti-rotating core within CPC 2 could confirm convection phenomena occurring in the atmosphere of Jupiter (Dowling & Gierasch, 1989; Smith et al., 1979) that would just appear in that cyclone because of the favorable physical conditions (i.e., higher values of humidity allow clouds to be tracked within this cyclone). In JIRAM images, the mean lower radiance of the darker features is due to thicker clouds and/or adiabatic cooled regions related to upwelling motions. Different radiances in JIRAM images could be related to different heights of the clouds. Following this idea and considering the dynamics of the well-known tropical cyclones on the Earth, the advection of air from the bottom layers to the top clouds occurs within the "eye" of the cyclone: this upwelling cools the air, which is then ejected in an "outflow" diverging from the eye of the cyclone. This outflow would then counter-rotate with respect to the lower clouds, the "spiral rain bands" extending at the bottom of the cyclone. Similarities of Jupiter's cyclones with Earth's cyclones have been already highlighted in Adriani et al. (2020).

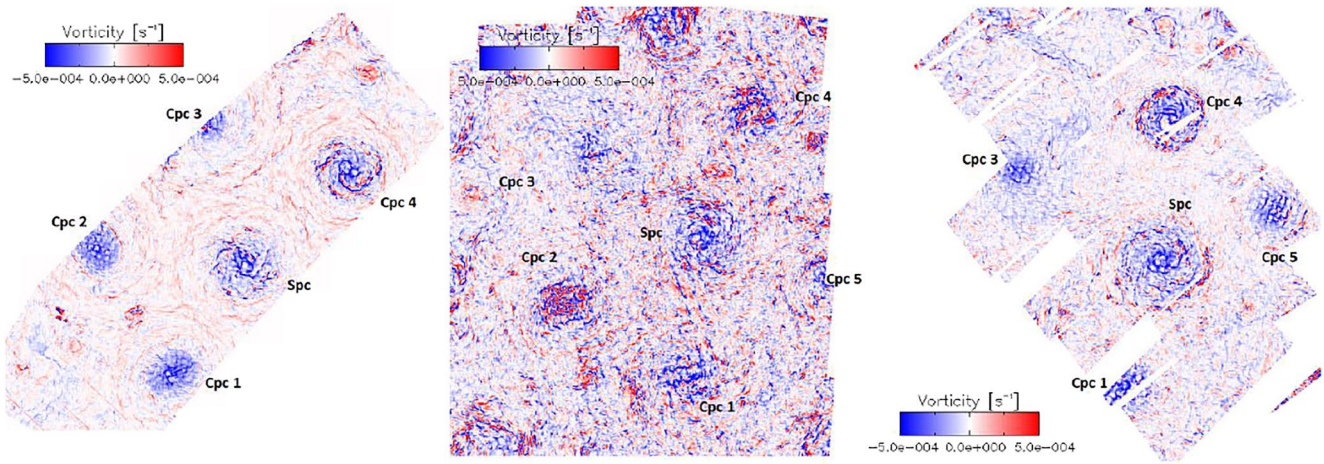

Figure 2. Mosaic of the vorticity maps obtained for PeriJove (PJ) 4 (left panel), PJ 30 (middle panel), and PJ 33 (right panel); positive values of vorticity correspond to antivorticity in the adopted notation. Vorticity in regions covered by multiple, overlapping pairs of sequences, is obtained as an average of the estimated vorticities. A 5×5 smoothing has been imposed. CPC means circumpolar cyclone; circumpolar cyclones are clockwise numbered. SPC means Southern Polar Cyclone.

Across the entire south polar region, we find smaller vortices characterized by anticyclonic motions. The majority of these anticyclones are found on the top of the vorticity map, at the left and right of CPC 3. However, the largest anticyclones are the two vortices at the left of CPC 1: one of them has a very low radiance, while the other one (closer to CPC 1), partially enveloped by bright clouds, shows a ring of opposite vorticity (cyclonic vorticity) partially encircling the anticyclonic inner region, in a similar manner—although reversed—to the cyclonic core-anticyclonic ring that we observe in the case of the main vortices.

Turbulent dynamics equatorward of −80° latitude are associated with a less regular pattern in the vorticity map. No general background can be recognized, although we must note that these regions are not within the focus of our study (our data selection is not meant to give proper spatial coverage of them). At the bottom of the vorticity map, intense winds locally form coherent regions of cyclonic and anticyclonic motions, that are not related to the main polar vortices.

We extended this study to different PJ passages. In Figure 2 we show vorticity maps for PJ 4, PJ 30, and PJ 33. The coverage in time allows us to evaluate the stability of the polar cyclones thanks to the derived vorticity maps on a 4 years' time frame (PJ 4 data set has been acquired in February 2017, PJ 33 data set in April 2021). At the same time, vorticity maps related to recent orbits (PJ 28 to PJ 33) allow us to estimate changes that occur on a shorter time scale (53 days is the time gap between each PJ passage).

The PJ 4 vorticity map is smoother than the other vorticity maps that we present. Vorticity and antivorticity motions in the PJ 4 vorticity map are well contrasted, while vorticity maps associated with the more recent orbits are noisier (especially PJ 30). In particular, the general anticyclonic vorticity field surrounding the main cyclones is more defined in the PJ 4 map than in the other vorticity maps. This different level of detail is related to the better spatial resolution and the larger time gap that we had between images acquired during PJ 4 (see Table 1), with respect to the other Juno orbits. For an evaluation of the effects induced by the time gap between images on the quality of vorticity maps, see the Appendix A.

The general structure of the polar cyclones is maintained along the PJ passages: the pentagon of CPCs is always present, although the entire structure rotated from PJ 4 until the more recent orbits of Juno spacecraft (Mura et al., 2021) and the angular distance between CPC 1 and CPC 5 widened during PJ 33.

The main cyclones are associated with cyclonic motions and are encircled by a slightly counter-rotating environment, which dominates the background poleward of −80°. The vorticity in both cyclones and the environment seems qualitatively similar along the PJ passages (apart from the already discussed differences between the PJ 4 map and the other PJs' maps), although local changes can be observed. Indeed, while the vorticity in the SPC does not change in time, in some cases the southern CPCs are affected by local changes in their structures and dynamics.

1. CPC 1 appears regular and almost circular and does not display strong variations in terms of vorticity.
2. CPC 2 displays its puzzling core during all recent orbits (8 months have passed between PJ 28 and PJ 33), but it did not show it during PJ 4. As already discussed, this feature may be induced by a very low radiance region.
3. CPC 3 is very irregular, almost oval in some cases; the double ring that we inferred in PJ 28 is also clear in PJ 4, PJ 30, and PJ 33. The inner, circular region, displays a stronger cyclonic motion, while the outer ring shows a weaker cyclonic motion (particularly clear during PJ 4). The fact that the first and the second ring are connected in the vorticity maps, suggests a typical core-arm structure, although the arm of this cyclone covers a very wide region, compared to the other main vortices.
4. CPC 4 displays some changes in its vorticity during PJ 30 and shows a behavior similar to CPC 2. However, the noise associated with this map does not allow us to draw any conclusions; moreover, also this region appears featureless and dark during this orbit. CPC 4 does not show any anticyclonic motions during the other orbits; thus, if the behavior reported in the PJ 30 map is real, it was only present during this orbit. During PJ 33, CPC 4 has a sudden increase in its radiance (not shown); however, this change in the measured radiance does not lead to a change in the local vorticity.
5. CPC 5 is smaller than the other southern CPCs. The antivorticity observed during PJ 28, which seemed to be related to the arm of this cyclone, is not present in any of the other Juno orbits. We must note that CPC 5 does not reach values of radiance as low as PJ 28 in any of these orbits.

Transient events, like the formation of anticyclonic structures, are observed in several cases along the PJ passages. PJ 4 has been acquired more than 4 years before PJ 30 and PJ 33 and does not help in the estimation of the lifespan of such features, which is much shorter. A visual comparison of the vorticity maps associated with the more recent orbits may be more useful: however, we did not find anticyclonic structures surviving for more than one PJ passage. For this reason, if we exclude a correlation between each of these events, we can estimate that the lifespan of these structures is far lower than 53 days (the period between two PJ passages). Indeed, we find ∼10 small anticyclones each PeriJove passage; all these events vanish from one Juno orbit to the other. Therefore, if we assume a similar lifetime for each of these features, we can give a rough estimation of ∼5 days of maximum lifespan.

In the hypothesis of circular symmetry, the radial distribution of radiance within the main cyclones gives an idea of the distribution of the clouds. In Figure 3 we show radial profiles of the radiance for different Juno orbits, for each of the CPCs and the SPC, obtained within a radius of 3,000 km from their centers. We only show PJ 4 (black line) and PJ 8 (blue line) as older orbits samples, and PJ 28 (green line) and PJ 30 (red line) as recent orbits samples.

Older orbits, like PJ 4 and PJ 8, display different radial profiles of the radiance with respect to recent orbits, like PJ 28 and PJ 30, both in CPC 4 and CPC 5. Indeed, while during recent orbits, these two CPCs show an increasing trend toward their peripheries, during older orbits they display two peaks at smaller radius (CPC 4) or one peak around 1,300–1,700 km (CPC 5). CPCs 2 and 3 have more stable radial profiles of the radiance along different orbits; indeed, in PJ 8, PJ 28, and PJ 30 they all show an increasing trend as the radius becomes larger, meanwhile, during PJ 4, the very same CPCs 2 and 3 radiance profiles peak around 2,000–2,300 km, where they grow larger by a factor of 2–3 with respect to the other PJ passages. No qualitative discrepancies can be noted in CPC 1 as well as in SPC, whose radiance behave similarly throughout all the Juno orbits (apart from the PJ 4 case, which shows a peak around 1,900 km, shifted with respect to the other orbits); SPC radiances peaks in general on the same level during all the orbits, suggesting similar cloudiness along time, with respect to the changes happening within the CPCs.

In PJ 28, as well as all recent Juno orbits, radial profiles of the radiance for all the southern CPCs increase as we move further from the center of the cyclone. This change in radiance occurs with an almost monotonic trend. Maximum in the radiance profiles is reached between 2,000 and 3,000 km from the center of each circumpolar cyclone. Radiance radial profiles behave similarly in all the southern CPCs and no qualitative differences can be deduced in their trends within recent orbits.

Although Figure 3 displays relevant changes in the structure of the main CPCs between older and recent orbits, these changes do not—in general—correspond to changes in vorticity maps. In particular, CPC 4 is prone to large and quick variations of its radiance profiles. Besides the change between PJ 4 and PJ 28, which we already described through the radial profiles of the radiance shown in Figure 3, CPC 4 also displayed a sudden and strong

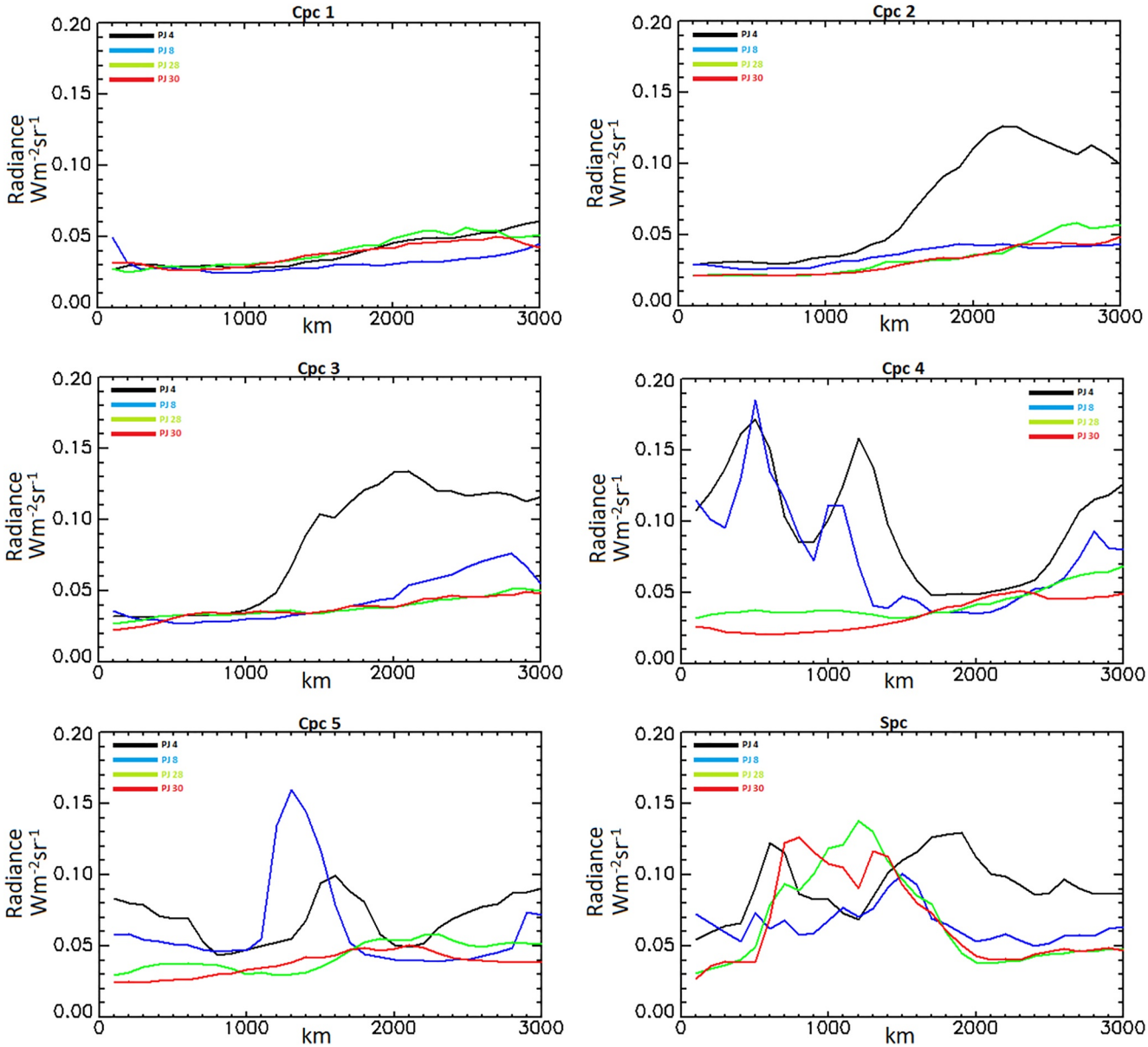

Figure 3. Radial profiles of the radiance for: (left upper panel) circumpolar cyclones (CPC) 1, (right upper panel) CPC 2, (left middle panel) CPC 3, (right middle panel) CPC 4, (left bottom panel) CPC 5, (right bottom panel) Southern Polar Cyclone. Each color corresponds to the radiance radial profile of a different PeriJove passage.

increase of its radiance during PJ 33. Both these changes in the radiance did not correspond to a change in the local vorticity field (see Figure 2).

5. Conclusions

JIRAM images acquired at the Jupiter's southern polar region have been processed to retrieve winds and—consequently—vorticity. Motions of the clouds have been retrieved by direct comparison of JIRAM images at different times. Only a subset of the whole data set has been used, due to the need for a satisfying spatial coverage and a minimum time gap of 8 min between images, necessary to minimize the noise. As a result of this study, we show vorticity maps for PJ 4, PJ 28, PJ 30, and PJ 33: a total of ~20 cyclones vorticity maps have been presented.

The vorticity field of a cyclone is a crucial quantity for the stability of the polar structure, according to different studies. In Li et al. (2020), the crucial parameter is the antivorticity field in between cyclones. In Gavriel and Kaspi (2021), formalism is ascribed to the gradient of the vorticity field. In both, the resultant effect is similar: the presence of a structure with higher vorticity in the center acts against the drift of further cyclones in the same region. For this reason, it is important to quantify the vorticity map over the largest possible area in the region poleward of ±80° of latitude, where the cyclones' dynamics occur (Adriani et al., 2017, 2020; Mura et al., 2021).

Recent observations of Jupiter cyclones show that any change in the structure (number of cyclones and/or shape) is an extremely unlikely event on an annual scale, which has only happened once, and only temporarily: a sixth cyclone joined the pentagonal structure in the South and formed a hexagonal structure, but it disappeared after a relatively short time, without merging with the pre-existing cyclones (Mura et al., 2021). Neither the merging of two cyclones nor the disappearance or creation of one stable cyclone has ever been observed. Instead, cyclones oscillate around equilibrium positions, and these oscillations tend to propagate from one cyclone to another, with an almost equal time scale.

Vortices originate through an inverse-cascade process, from small-scale turbulences. Cyclones rotate clockwise and anticlockwise respectively in the southern and northern hemispheres, and migrate westward-poleward (β-drift effect), due to the interaction with the vorticity background.

The two (North and South) regular structures do perform a slow westward drift around their respective poles (Mura et al., 2021), but the drift is extremely slow for the oscillations that should be ascribed to the β-drift effect and is characterized by significantly different angular velocities, which suggests that deep differences exist in the North and the South pole atmosphere. In fact, neither Li et al. (2020) nor Gavriel and Kaspi (2021) accounted for baroclinicity, so they cannot explain the slow drift. That will require more complex modeling.

We confirm that, in agreement with the prediction of Li et al. (2020), O'Neill et al. (2015) and Brueshaber et al. (2019), the main south polar cyclones (negative-blue in our notation) are embedded in a general anticyclonic vorticity field (positive-red in the maps). This dichotomy, although more appreciable in the PJ 4 map (due to the better spatial coverage and longer time gap), is still present after 4 years of observations, demonstrating the general stability of the Jupiter southern polar cyclonic system. The presence of an anticyclonic vorticity field surrounding the main polar cyclones acts as shielding for the cyclones, denying their merging and the breaking of the structure.

A crucial result of this study is that, both in the morphology (maps of radiance and hence of clouds coverage) and in the winds (maps of the vorticity field), differences occur between cyclones, and these differences are quite stable over time. This raises a concern on those models based on equal cyclones for achieving the equilibrium, such as Gavriel and Kaspi (2021), or more intriguing, suggests that the dynamics of cyclones is only partially correlated with the topmost velocity field that we can observe. In Gavriel and Kaspi (2021), they made use of JIRAM data as input for a model of polar cyclones' stability and number; they used data from Grassi et al. (2018), related to the central cyclone of each pole. In this study we use the same data of Grassi et al. (2018) and we note that every cyclone has its own vorticity distribution, so that the radial profile of velocity should differ from cyclone to cyclone. Another crucial point is that, while Gavriel and Kaspi (2021) assume that the South CPCs are larger than the polar one, we observe the contrary, as already reported by Adriani et al. (2020).

No strong correlation has been found between cloudiness (radiance) and vorticity in the Jupiter southern polar region. Changes in the radiance radial profiles of CPCs, between one orbit and the other, do not always reflect changes in the vorticity maps. CPC 2 is an exception: during the more recent orbits, it displays a very noisy core corresponding to its inner and darker region, which was not present during PJ 4. This core presents both anticyclonic and cyclonic features. On the contrary, a visual inspection of JIRAM images reveals no bright features within this cyclone.

The analysis of CPC 2 has been conducted through both observations of the vorticity map and of its radial profile of the radiance and vorticity. In general, the core of this cyclone shows featureless dark clouds; thus, winds are difficult to retrieve within the core of CPC 2. Further analysis would require an evaluation of the

content of several minor species within the CPC 2; however, such a study has not been possible. Cloud opacity in the region of cyclones is usually rather high, and consequently, the methods presented in Grassi et al. (2018, 2020) have limited applicability. A direct inspection of the available spectral coverage has demonstrated that no spectra corresponding to areas with $\tau < 2$ were acquired over the southern CPC 2 during PJ 28–PJ 33 passages.

The assessment of the stability of cyclones at Jupiter's poles will benefit from a prolonged study in the next Juno orbits. JIRAM observations have covered more than 4 years until now. Having a longer time frame covered by observations would permit us to evaluate the stability of the cyclonic regions of Jupiter on a longer time scale and would be useful to test models. Models have been vastly adopted in the study of planetary atmospheres, even in the case of Jupiter, and will play a role complementary to observations in the understanding of the physical mechanisms happening within Jupiter's atmosphere.

Appendix A

Data selection (imposed considering a minimum time gap between images) and the optimization of the search area had a dramatic effect on the vorticity maps that we produced. Here (Figure A1) is shown the example of the PJ 28 vorticity map for two different cases:

1. (left) images mainly separated by 4 min, 21 × 21 search area around each pixel neighborhood;
2. (right) images separated by 8 min, 41 × 41 search area around each pixel neighborhood.

The left map, obtained for the shortest available time gap between images acquired by Jovian InfraRed Auroral Mapper during PJ 28, is noisier than the one on the right, derived on a more selected data set. Imposing a time gap of 8 min clearly affects the quality of the map. A bright strip crosses the left map between circumpolar cyclone (CPC) 3, CPC 4 and the Southern Polar Cyclone (SPC); this patchy behavior is due to the only

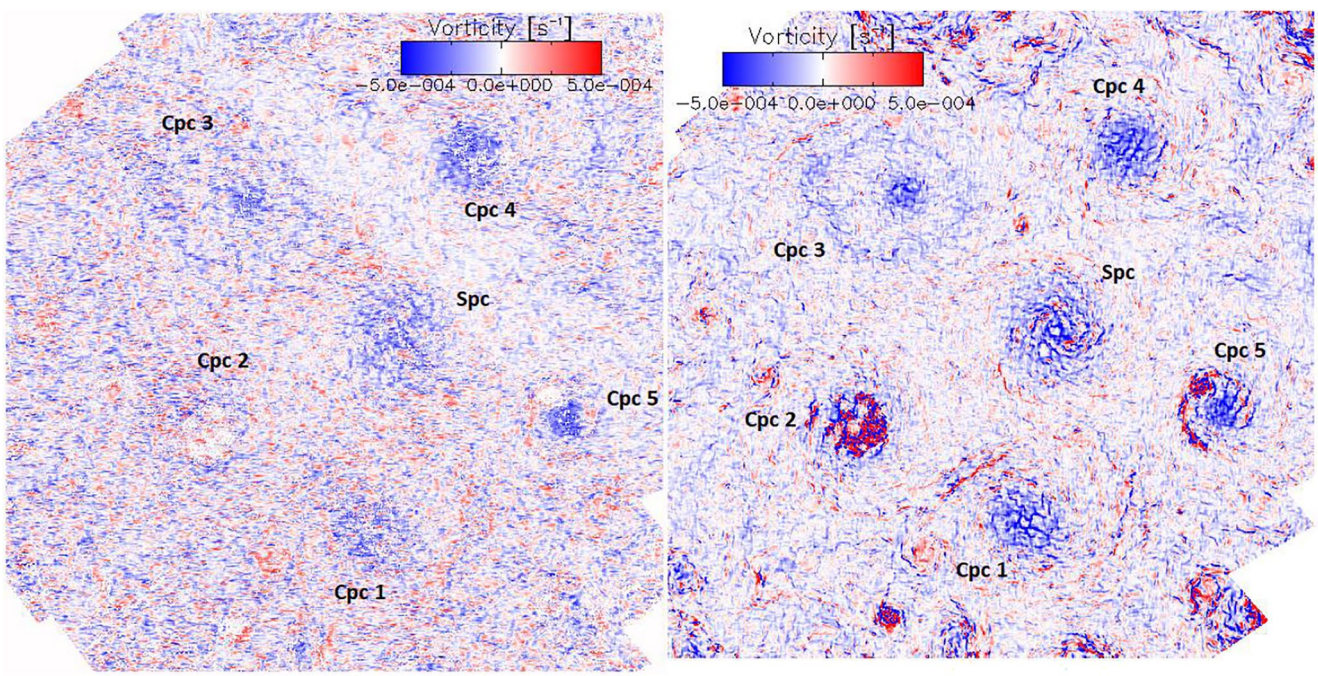

Figure A1. (Left) time gap of 4 min between different images, 21 × 21 search area; (right) time gap of 8 min between different images, 41 × 41 search area. A 5 × 5 smoothing has been imposed.

region—of this map—obtained by comparison of images separated by 8 min. Beside this region, all the left map is made of images separated by 4 min. The majority of the small-scale structures do not emerge over the noisy background.

The presence of white spots within the CPC 2 core and the CPC 5 arm is due to the size of the search area. These are spurious regions that occur because of the incapability of the algorithm to retrieve the best matching vector within such a small search area. Indeed, whenever a best matching vector is not found within the area, the algorithm assumes the radius of the search area itself as the best matching vector. Thus, a coherent region characterized by the same displacement vector—that means the same velocity vector—is associated with a local null vorticity (being the vorticity the curl of the velocity field). Increasing both the search area and the time gap removed these effects and produced the maps that we have shown in this paper.

The general stability of the polar vortices could also be evaluated thanks to the latitudinal profiles of the vorticity (Figure A2), obtained for several PeriJove passages: the analysis of data over a long-time interval, could allow to better study the stability of the vortices. However, it must be noted that only PJ 28 covers all the latitudes poleward of −80°. Moreover, the SPC displacement with respect to the geographical south pole, makes it difficult to give a straightforward interpretation of these profiles.

In general, PJ 28 latitudinal profile of the vorticity obtained with respect to the geographical pole shows an average vorticity about $-3.5 * 10^{-5}$ s^{-1}. The minimum at −88° is due to the SPC cyclonic circulation, while the local maximum at −86° is related to the anticyclonic ring surrounding this cyclone. Between −82.5° and −84.5° the profile is sensible to the southern circumpolar cyclones.

PJ 28 latitudinal profile of the vorticity is in general dominated by the cyclonic circulation. This is a direct consequence of the southern polar and circumpolar cyclones. A similar result was obtained in Garcia et al. (2020) in both their simulations. However, being the focus of our work about the south polar region, we cannot extend the comparison to latitudes equatorward of −80°.

Figure A2 shows also the PJ 28 latitudinal profile of the vorticity obtained with respect to the center of SPC. In this case, the latitudinal profile spans a wider range of values. Moreover, the minimum at −90° (which is in this case by definition related to the SPC) is more recognizable, as well as the effect of the CPCs between −84° and −85°.

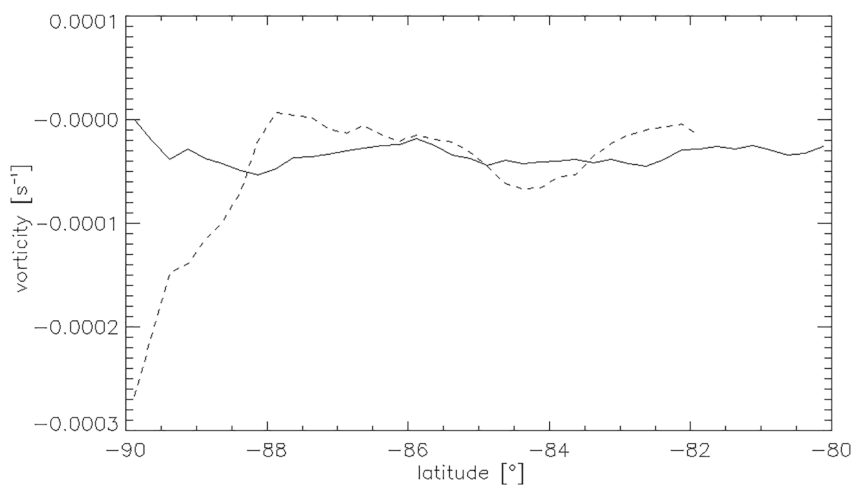

Figure A2. Latitudinal profile of the vorticity obtained with respect to the geographical pole (solid line) and the center of Southern Polar Cyclone (dashed line).

Data Availability Statement

JIRAM data used in this study (Noschese & Adriani, 2017a, 2017b) is publicly available on the NASA Planetary Data System (https://pds-atmospheres.nmsu.edu/data_and_services/atmospheres_data/JUNO/jiram.html). The individual datasets are available at https://atmos.nmsu.edu/PDS/data/jnojir_XXXX, where xxxx is 1004, 1028, 1030 or 1033 for EDR (Experiment Data Record; raw data) and 2004, 2028, 2030 or 2033 for RDR (Reduced Data Record; calibrated data) volumes. All the ".img" and ".lbl" files that have been used in this work, are reported in a repository (Scarica, 2022; https://doi.org/10.5281/zenodo.6762715).

Acknowledgments
This work was supported by the Italian Space Agency (ASI) through ASI-INAF agreement n. 2016-23-H.0 and its addendum n. 2016-23-H.1-2018 and n. 2016-23-H.2-2021. Open Access Funding provided by Istituto nazionale di astrofisica within the CRUI-CARE Agreement.

References

Adriani, A., Bracco, A., Grassi, D., Moriconi, M. L., Mura, A., Orton, G., et al. (2020). Two-year observations of the Jupiter polar regions by JIRAM on board Juno. *Journal of Geophysical Research: Planets*, *125*(6), e06098. https://doi.org/10.1029/2019JE006098

Adriani, A., Filacchione, G., Di Iorio, T., Turrini, D., Noschese, R., Cicchetti, A., et al. (2017). JIRAM, the Jovian infrared auroral mapper. *Space Science Reviews*, *213*(1–4), 393–446. https://doi.org/10.1007/s11214-014-0094-y

Adriani, A., Mura, A., Orton, G., Hansen, C., Altieri, F., Moriconi, M. L., et al. (2018). Clusters of cyclones encircling Jupiter's poles. *Nature*, *555*(7695), 216–219. https://doi.org/10.1038/nature25491

Baines, K. H., Momary, T. W., Fletcher, L. N., Showman, A. P., Roos-Serote, M., Brown, R. H., et al. (2009). Saturn's north polar cyclone and hexagon at depth revealed by Cassini/VIMS. *Planetary and Space Science*, *57*(14–15), 1671–1681. https://doi.org/10.1016/j.pss.2009.06.026

Baines, K. H., Simon-Miller, A. A., Orton, G. S., Weaver, H. A., Lunsford, A., Momary, T. W., et al. (2007). Polar lightning and decadal-scale cloud variability on Jupiter. *Science*, *318*(5848), 226–229. https://doi.org/10.1126/science.1147912

Bolton, S. J., Adriani, A., Adumitroaie, V., Allison, M., Anderson, J., Atreya, S., et al. (2017). Jupiter's interior and deep atmosphere: The initial pole-to-pole passes with the Juno spacecraft. *Science*, *356*(6340), 821–825. https://doi.org/10.1126/science.aal2108

Brueshaber, S. R., Sayanagi, K. M., & Dowling, T. E. (2019). Dynamical regimes of giant planet polar vortices. *Icarus*, *323*, 46–61. https://doi.org/10.1016/j.icarus.2019.02.001

Cai, T., Chan, K. L., & Mayr, H. G. (2021). Deep, closely packed, long-lived cyclones on Jupiter's poles. *The Planetary Science Journal*, *2*(2), 81. https://doi.org/10.3847/PSJ/abedbd

Carlson, R. W., Weissman, P. R., Smythe, W. D., & Mahoney, J. (1992). Near-infrared mapping spectrometer experiment on Galileo. *Space Science Reviews*, *60*(1–4), 457–502. https://doi.org/10.1007/BF00216865

Coradini, A., Filacchione, G., Capaccioni, F., Cerroni, P., Adriani, A., Brown, R., et al. (2004). CASSINI/VIMS-V at Jupiter: Radiometric calibration test and data results. *Planetary and Space Science*, *52*(7), 661–670. https://doi.org/10.1016/j.pss.2003.11.005

Dowling, T. E., & Gierasch, P. J. (1989). Cyclones and moist convection on Jovian planets. *Bulletin of the American Astronomical Society*, *21*, 946.

Garcia, F., Chambers, F. R. N., & Watts, A. L. (2020). Deep model simulation of polar vortices in gas giant atmospheres. *Monthly Notices of the Royal Astronomical Society*, *499*(4), 4698–4715. https://doi.org/10.1093/mnras/staa2962

Gavriel, N., & Kaspi, Y. (2021). The number and location of Jupiter's circumpolar cyclones explained by vorticity dynamics. *Nature Geoscience*, *14*(8), 559–563. https://doi.org/10.1038/s41561-021-00781-6

Gonzalez, R. C., & Woods, R. E. (2008). *Digital image processing* (3rd ed.). Prentice Hall.

Grassi, D., Adriani, A., Moriconi, M. L., Mura, A., Tabataba-Vakili, F., Ingersoll, A., et al. (2018). First estimate of wind fields in the Jupiter polar regions from JIRAM-Juno images. *Journal of Geophysical Research: Planets*, *123*(6), 1511–1524. https://doi.org/10.1029/2018JE005555

Grassi, D., Adriani, A., Mura, A., Atreya, S. K., Fletcher, L. N., Lunine, J. I., et al. (2020). On the spatial distribution of minor species in Jupiter's troposphere as inferred from Juno JIRAM data. *Journal of Geophysical Research: Planets*, *125*(4), e06206. https://doi.org/10.1029/2019JE006206

Guervilly, C., & Hughes, D. W. (2017). Jets and large-scale vortices in rotating Rayleigh-Bénard convection. *Phys. Rev. Fluids*, *2*(11), 113503. https://doi.org/10.1103/PhysRevFluids.2.113503

Hueso, R., Sánchez-Lavega, A., Iñurrigarro, P., Rojas, J. F., Perez-Hoyos, S., Mendikoa, I., et al. (2017). Jupiter cloud morphology and zonal winds from ground-based observations before and during Juno's first PJ. *Geophysical Research Letters*, *44*(10), 4669–4678. https://doi.org/10.1002/2017GL073444

Ingersoll, A., Ewald, S. P., Tosi, F., Adriani, A., Mura, A., Grassi, D., et al. (2021). Polygonal patterns of cyclones on Jupiter: Convective forcing and anticyclonic shielding. https://doi.org/10.21203/rs.3.rs-388198/v1

Li, C., Ingersoll, A. P., Klipfel, A. P., & Brettle, H. (2020). Modeling the stability of polygonal patterns of vortices at the poles of Jupiter as revealed by the Juno spacecraft. *Proceedings of the National Academy of Sciences*, *117*(39), 24082–24087. https://doi.org/10.1073/pnas.2008440117

Mura, A., Adriani, A., Altieri, F., Connerney, J. E. P., Bolton, S. J., Moriconi, M. L., et al. (2017). Infrared observations of Jovian aurora from Juno's first orbits: Main oval and satellite footprints. *Geophysical Research Letters*, *44*(11), 5308–5316. https://doi.org/10.1002/2017GL072954

Mura, A., Adriani, A., Bracco, A., Moriconi, M. L., Grassi, D., Plainaki, C., et al. (2021). Oscillations and stability of the Jupiter polar cyclones. *Geophysical Research Letters*, *48*(14), e94235. https://doi.org/10.1029/2021GL094235

Noschese, R., & Adriani, A. (2017a). JNO-J-JIRAM-2-EDR-V1.0. Nasa Planetary Data System. Retrieved from https://pds-atmospheres.nmsu.edu/data_and_services/atmospheres_data/JUNO/jiram.html

Noschese, R., & Adriani, A. (2017b). JNO-J-JIRAM-3-RDR-V1.0. Nasa Planetary Data System. Retrieved from https://pds-atmospheres.nmsu.edu/data_and_services/atmospheres_data/JUNO/jiram.html

O'Neill, M. E., Emanuel, K. A., & Flierl, G. R. (2015). Polar vortex formation in giant-planet atmospheres due to moist convection. *Nature Geoscience*, *8*(7), 523–526. https://doi.org/10.1038/ngeo2459

Reuter, D. C., Simon-Miller, A. A., Lunsford, A., Baines, K. H., Cheng, A. F., Jennings, D. E., et al. (2007). Jupiter cloud composition, stratification, convection, and wave motion: A view from new horizons. *Science*, *318*(5848), 223–225. https://doi.org/10.1126/science.1147618

Rubio, A. M., Julien, K., Knobloch, E., & Weiss, J. B. (2014). Upscale energy transfer in three-dimensional rapidly rotating turbulent convection. *Physical Review Letters*, *112*(14), 144501. https://doi.org/10.1103/PhysRevLett.112.144501

Scarica, P. (2022). Repository for the paper "Stability of the Jupiter southern polar vortices inspected through vorticity using Juno/JIRAM data" [Dataset]. Zenodo. https://doi.org/10.5281/zenodo.6762715

Schecter, D. A., & Dubin, D. H. E. (1999). Vortex motion driven by a background vorticity gradient. *Physical Review Letters*, *83*(11), 2191–2194. https://doi.org/10.1103/PhysRevLett.83.2191

Siegelman, L., Klein, P., Ingersoll, A., Ewald, S., Young, W., Bracco, A., et al. (2021). Moist convection drives an upscale energy transfer at Jovian high latitudes. *Nature Physics*. https://doi.org/10.21203/rs.3.rs-440902/v1

Smith, B. A., Soderblom, L. A., Beebe, R., Boyce, J., Briggs, G., Carr, M., et al. (1979). The Galilean satellites and Jupiter: Voyager 2 imaging science results. *Science*, *206*(4421), 927–950. https://doi.org/10.1126/science.206.4421.927

Vallis, G. K. (2017). *Atmospheric and oceanic fluid dynamics*. Cambridge University Press. https://doi.org/10.1017/9781107588417

Yadav, R. K., Heimpel, M., & Bloxham, J. (2020). Deep convection–driven vortex formation on Jupiter and Saturn. *Science Advances*, *6*(46), eabb9298. https://doi.org/10.1126/sciadv.abb9298

Yanai, M. (1964). Formation of tropical cyclones. *Reviews of Geophysics*, *2*, 367–414. https://doi.org/10.1029/RG002i002p00367